



Phosphorus modification to improve the hydrothermal stability of a Cu-SSZ-13 catalyst for selective reduction of NO_x with NH₃

Huawang Zhao^a, Yingnan Zhao^b, Mengke Liu^a, Xianghui Li^a, Yuhan Ma^a, Xin Yong^a, Hong Chen^c, Yongdan Li^{a,b,*}

^a Collaborative Innovation Center of Chemical Science and Engineering (Tianjin), Tianjin Key Laboratory of Applied Catalysis Science and Technology, State Key Laboratory of Chemical Engineering (Tianjin University), School of Chemical Engineering, Tianjin University, Tianjin, 300072, China

^b Department of Chemical and Metallurgical Engineering, School of Chemical Engineering, Aalto University, Espoo, 02150, Finland

^c School of Environmental Science and Engineering, Tianjin University, Tianjin, 300072, China

ARTICLE INFO

Keywords:

Cu-SSZ-13
NH₃-SCR
Hydrothermal aging
Phosphorus modification
Emission control

ABSTRACT

Phosphorus is introduced to modify the Cu-SSZ-13 catalyst via incipient wetness impregnation, with P/Cu-SSZ-13 = 1 and 2 wt.%, and Si/Al = 4, for selective catalytic reduction of NO_x with NH₃. N₂ physisorption and XRD results show the incorporation of phosphorus as phosphate acid enhanced the hydrothermal stability of Cu-SSZ-13 significantly, during hydrothermal aging in 10 vol.% H₂O/air at 750 °C for 16 h. NMR and Raman results suggest that phosphate ions migrate and coordinate with the framework-bonded Al species, forming a framework silicoaluminophosphate interface, thus impeding further dealumination and structure collapse. Before the hydrothermal aging, the isolated Cu²⁺ ions partly interact with the phosphate ions, forming Cu-phosphate species and reducing the SCR performance. Nevertheless, the appropriate content of phosphate ions can prevent the structure collapse caused by the hydrothermal aging, remaining the isolated Cu²⁺ ions as well as excellent SCR performance.

1. Introduction

Various catalytic technologies have been developed to eliminate the emission of engines [1–3]. For diesel vehicles, the emission of hydrocarbons and carbon monoxide is controlled by a diesel oxidation catalyst, whereas the particulate matter is removed with a diesel particulate filter (DPF) [4]. Subsequently, nitrogen oxides (NO_x) can be removed with either a lean NO_x trap for light-duty vehicles, or a NH₃ selective catalytic reduction (NH₃-SCR) unit for heavy-duty ones [5,6]. Typically, the DPF requires regeneration in hot vapor at above 650 °C, inducing hydrothermal condition to the SCR catalysts in the downstream [7–9]. Therefore, a high hydrothermal durability is required for the SCR catalyst to achieve effective NO_x emission control [9–13].

Cu-CHA (Cu-CHA) zeolites, including Cu-SSZ-13 and Cu-SAPO-34, have been successfully commercialized as catalysts for NH₃-SCR reaction, to meet the stringent standards for diesel NO_x emission in both North America and Europe, marking a significant breakthrough of catalytic technology in recent years [14–16]. Better hydrothermal stability has been shown with the Cu-CHA catalysts, as compared to the other zeolite-based catalysts, e.g., Cu-ZSM-5, Cu-Beta and Cu-Y [17]. One well-accepted explanation is that the unique topology and the

small pore size in Cu-CHA zeolites prevent the detached Al(OH)₃ moieties from escaping the CHA cavity [4,11].

Cu-SSZ-13 has been found inferior to Cu-SAPO-34 in the hydrothermal stability [18,19]. For the next generation Cu-SSZ-13 catalyst, stronger hydrothermal stability should be achieved to prolong the lifetime and lower the cost [17,20–23]. One approach is to maintain the content of two adjacent framework Al sites (Al pairs), such as Al-O-Si-O-Al or Al-O-(Si-O)₂-Al, stabilizing the isolated Cu²⁺ active sites in the six-membered rings (6MR) in the catalyst under hydrothermal conditions [24–28]. High content of the Al pairs requires a low Si/Al ratio, typically below 6 [22,29,30]. Nevertheless, the framework of the zeolite can be collapsed more easily with the low Si/Al ratio, caused the hydrothermal condition [31].

Phosphorus (P) is well known for improving the hydrothermal stability of H-ZSM-5 as well as the other zeolites with similar multi-dimensional 10 MR structures, such as ZSM-11, MCM-22, ITQ-13 and IM-5 [32–36]. Meanwhile, phosphorus in SAPO-34 has been proposed critical to stabilize the CHA type framework in hydrothermal condition [37]. It is therefore interesting to investigate the effect of P on the hydrothermal stability of the other CHA type catalyst, i.e. Cu-SSZ-13 with a low Si/Al ratio.

* Corresponding author.

E-mail address: yongdan.li@aalto.fi (Y. Li).

In this work, phosphorous is incorporated to modify the Cu-SSZ-13 catalyst with Si/Al ratio = 4. The effect of phosphorus on the framework structure, the cupric sites and the SCR performance will be discussed.

2. Experimental

2.1. Chemicals

Copper(II) sulfate (CuSO_4 < 99 wt.-%), sodium aluminate (NaAlO_2 < 98 wt.-%) and phosphoric acid (80 wt.-%) were purchased from Guangfu (Tianjin). Tetraethylenepentamine (TEPA < 98 wt.-%) and sodium hydroxide (NaOH < 98 wt.-%) were purchased from Aladdin Industrial Corporation (Shanghai). Ammonium nitrate (NH_4NO_3 < 99 wt.-%) was purchased from Yuanli (Tianjin). Colloidal silica (JN-30, SiO_2 = 30 wt.-%) was purchased from Haiyang (Qingdao). All the aqueous solutions were prepared using ultra-pure water purchased from Yongqingyuan (Tianjin).

2.2. Catalyst preparation

The Cu-SSZ-13 was synthesized with one-pot hydrothermal synthesis using copper-tetraethylenepentamine (Cu-TEPA) as a structure-directing agent [38]. About 180 ml gel was prepared with a molar ratio of 2.5 Na_2O :1 Al_2O_3 :10 SiO_2 :150 H_2O :2 Cu-TEPA and then transferred into a 250 ml autoclave with a Teflon liner and crystallized at 140 °C for 96 h. The solid product was filtrated and washed with water, and then dried at 100 °C overnight. 15 g of the dried powder was immersed in 300 ml NH_4NO_3 solution (1 mol/L) at 80 °C and kept for 6 h for ion exchange. The sample was then filtrated, washed and dried at 100 °C, followed by calcination in synthetic air at 600 °C for 6 h. The details of the synthesis for SSZ-13 and preparation of the H-SSZ-13 were shown in Sections 1 and 2 in Supporting Information.

The P doped Cu-SSZ-13 catalysts (P/Cu-SSZ-13 = 1 wt.-%, 2 wt.-% and 5 wt.-%) were prepared with incipient wetness impregnation. The solution content in the impregnation was determined with the pre-tested water-absorption of the dry sample. Typically, 0.6 ml phosphoric acid solution with different concentrations (0.51, 1.02 and 2.55 mol/L) was dropped onto 1 g of the prepared Cu-SSZ-13, obtaining the catalysts with 1 wt.-%, 2 wt.-% and 5 wt.-% P loading, respectively. The wetted catalyst was first dried at ambient conditions for 12 h, followed by drying at 100 °C overnight. Finally, the sample was calcined in synthetic air at 550 °C for 4 h. The fresh samples were hydrothermally aged in synthetic air flow containing 10% H_2O at 750 °C for 16 h. In order to figure out the performance of the P doped Cu-SSZ-13 after hydrothermal treatment at low temperatures, Cu-SSZ-13, P_1Cu and P_2Cu were hydrothermally treated at 70 °C for 16 h with 30 vol.-% moisture. All the catalysts were pelletized, crushed and sieved to 40–60 mesh before testing. Within the context of this article, the sample notations will be used as shown in Table 1.

Table 1
Sample notations and details of preparation procedure^a.

Samples	Preparation procedure
Cu-SSZ-13	Prepared with one-pot method and then ion-exchanged with NH_4NO_3 solution
P_1Cu	Cu-SSZ-13 impregnated with H_3PO_4 solution, containing 1 wt.-% P in the catalyst
P_2Cu	Cu-SSZ-13 impregnated with H_3PO_4 solution, containing 2 wt.-% P in the catalyst
P_5Cu	Cu-SSZ-13 impregnated with H_3PO_4 solution, containing 5 wt.-% P in the catalyst
Cu-H	Cu-SSZ-13 hydrothermal aged in 10% H_2O /air flow at 750 °C for 16 h
$\text{P}_1\text{Cu-H}$	P_1Cu hydrothermal aged in 10% H_2O /air flow at 750 °C for 16 h
$\text{P}_2\text{Cu-H}$	P_2Cu hydrothermal aged in 10% H_2O /air flow at 750 °C for 16 h

a. Note that the P_1Cu and P_2Cu samples are collectively named P_xCu . The $\text{P}_1\text{Cu-H}$ and $\text{P}_2\text{Cu-H}$ samples are denoted as $\text{P}_x\text{Cu-H}$.

2.3. Standard NH_3 -SCR test

The activity of the catalysts for NH_3 -SCR was tested in a fixed-bed quartz reactor (10 mm in diameter) in steady flow operation. Possible reactions are shown in Equations 1&2:



Typically, 50 mg of the catalyst (40–60 mesh) was mixed with 950 mg quartz sand and packed in the plug flow reactor, and the temperature was controlled by a type K thermocouple inserted into the center of the catalysts bed. The catalyst was activated in reactant gas (shown in below) flow at 550 °C for 1 h before the SCR performance test. The gas flow was kept at 500 ml/min (50 mg of catalyst corresponds to gas hourly space velocity = 300, 000 h^{-1}) during reaction. The reactant gas contains 500 ppm NO, 500 ppm NH_3 , 5 vol.-% O_2 , 5 vol.-% H_2O and N_2 as balance. For each run of testing, the reaction temperature was increased from 150 °C to 550 °C with step of 25 °C or 50 °C. At each step, the concentration of the products (NO, N_2O and NO_2) were recorded on FTIR (Thermo Nicolet iS10) with a 2 m gas cell when the reaction reached steady state (the concentration of the products changed less than 1 ppm in ten minutes). The NO_x ($\text{NO}_x = \text{NO} + \text{NO}_2$) conversion was calculated with Eq. (3):

$$\text{NO}_x \text{ conversion} = \left(1 - \frac{[\text{NO}_x]_{\text{out}}}{[\text{NO}_x]_{\text{in}}} \right) \times 100\% \quad (3)$$

2.4. Characterization

N_2 physisorption at -196 °C was used to determine the specific surface area and pore volume of the catalysts on Quantachrome Autosorb-1, with pre-degassing at 300 °C for 6 h. The specific surface area was calculated using BET equation and the pore volume was estimated using t-plot method.

The contents of the samples were determined via ICP-OES (VISTA-MPX, Varian). Before the ICP measurement, we treated the sample in 20% O_2/N_2 at 300 °C for 1 h to totally remove the adsorbed water in the zeolite. The crystallization structure was measured via XRD (Rigaku, D/max- γ b-type X-ray) using monochromatic $\text{Cu K}\alpha$ radiation (40 kV and 100 mA), with a scan speed of 2°/min. 20 mg sample was used of each measurement. The relative crystallinity of the catalysts was estimated based on the method proposed by Yamanaka et al. [39], using peak intensities at $2\theta = 9.4, 20.5$ and 30.4 ° and the as-prepared Cu-SSZ-13 as a reference, with Eq. (4):

$$\text{Relative crystallinity} = \frac{\text{the sum of the intensities of the peaks at } 2\theta = 9.4, 20.5 \text{ and } 30.4 \text{ } (\%) = \frac{\text{after treatment}}{\text{the sum of the intensities of the peaks at } 2\theta = 9.4, 20.5 \text{ and } 30.4 \text{ before treatment}} \times 100\% \quad (4)$$

^{27}Al and ^{31}P solid-state MAS NMR were conducted on Varian Infinity plus 300 WB spectrometer utilizing a 4 mm triple resonance probe operating with the resonance frequencies of 78.13 MHz and 121.37 MHz, respectively. Spectra of ^{27}Al were acquired by using calibrated ^{27}Al $\pi/20$ pulses of 0.5 μs , a 40 kHz spectral window, a spinning speed of 8 kHz, and a 3 s pulse delay. ^{31}P MAS NMR was conducted with a 40 kHz spectral window, a spinning speed of 9 kHz, and a 15 s pulse delay. $\text{Al}(\text{NO}_3)_3$ aqueous solution (1 mol/L) was used for ^{27}Al MAS NMR spectroscopy, and H_3PO_4 aqueous solution (75 wt.%) was used for ^{31}P MAS NMR spectroscopy, respectively, as references. Note that the NMR test condition and the sample amount are the same for all the samples. Hence, the NMR resonance intensity can be compared in each sample. The quantitative spectral analysis of the ^{27}Al MAS NMR results was performed by fitting the spectra with mixed Gaussian/Lorentzian line shapes using the Peakfit software. All samples allow the fitting parameters in the deconvolution to be optimized.

The Raman spectra were acquired with a Thermo Fisher Scientific DXR spectrometer with an excitation wavelength of 532 nm.

EPR spectra in the X-band were recorded with a CW spectrometer JES-FA200 with a microwave power of 1 mW modulation frequency of 100 kHz. The EPR signals of isolated Cu^{2+} ions were recorded at -150 °C with the magnetic field being swept from 2000 to 4000 G with a sweep time of 5 min.

The H_2 -TPR measurements were performed with an AutoChem 2920 apparatus with a TCD detector. 50 mg sample was heated to 550 °C in the 5% O_2/N_2 for 1 h before the H_2 -TPR test. After cooling down to room temperature, the sample was exposed to a flow of 5% H_2/N_2 , and the temperature was increased at a rate of 10 °C/min until 800 °C. The different cupric species were assessed by deconvolution of the H_2 -TPR curves with Gaussian peak shapes, using the variable line shape for each respective peak across all samples and allowing the fitting parameters in the deconvolution software to be optimized.

3. Results

3.1. Effect of phosphorus on the SCR performance

The activity of the as-prepared and doped Cu-SSZ-13 was compared in Fig. 1a. The NO_x conversion was around 20% with the as-prepared Cu-SSZ-13 at 150 °C, and increased rapidly to 78% at 200 °C. The conversion remained above 90% from 250 to 450 °C, then decreased with the further increase of the temperature, to approximately 77% NO_x conversion at 550 °C. The P loading caused decrease of the activity

at low temperatures, with the NO_x conversion of only 67% and 56% at 200 °C for the P_1Cu and P_2Cu samples, respectively. Nevertheless, the P doped catalysts (P_1Cu and P_2Cu) remained high activity at high temperatures, maintaining over 85% conversion even at 550 °C. The high P loading (5 wt.%) decreases the de NO_x activities significantly in 150–550 °C, with only around 50% NO_x conversion at 350 °C. This indicates that the high loading of P deactivated the Cu-SSZ-13 seriously, consistent with the previous works [40,41].

The activities of the aged catalysts are plotted in Fig. 1b to compare the hydrothermal stability. The Cu-SSZ-13 catalyst without P doping showed less than 10% conversion at 150 °C, and reached only 20% conversion for the maximum from 150 °C to 550 °C. In contrast, P-doped aged catalysts ($\text{P}_1\text{Cu-H}$ and $\text{P}_2\text{Cu-H}$) exhibited similar de NO_x activity below 250 °C with a NO_x conversion of around 40% at 200 °C, and maintained above 75% conversion in 250–500 °C. The doped catalyst with a higher P amount ($\text{P}_2\text{Cu-H}$) still got around 70% conversion at 550 °C, whereas only around 55% NO_x conversion remained in the $\text{P}_1\text{Cu-H}$. Apparently, the activity of the hydrothermally aged samples increased with the amount of P loading for the P_1Cu and P_2Cu samples.

A low temperature hydrothermal treatment (70 °C for 16 h with 30% H_2O in air) has little effect on the SCR performance of the Cu-SSZ-13 and P doped samples, as derived from the comparing of Fig. 1a and c.

3.2. Effects of phosphorus on Cu-SSZ-13 structure

3.2.1. Textural properties and X-ray diffraction

The chemical composition and Si/Al ratios are almost identical in all the samples before and after the hydrothermal aging, according to the ICP results listed in Table 2. The data in Table 3 show a slight decrease of the surface area and the pore volume with phosphorus incorporation (P_1Cu and P_2Cu) as compared to the as-prepared Cu-SSZ-13. The Cu-H sample without phosphorus lost almost all the pore volume and surface area after the hydrothermal aging. In contrast, the $\text{P}_1\text{Cu-H}$ and $\text{P}_2\text{Cu-H}$ samples with phosphorus remained around 70% of the surface area as well as around 80% of the pore volume after the hydrothermal aging, as compared to their fresh counterparts.

As shown in Fig. 2, XRD results show that the Cu-SSZ-13 and P doped samples show a typical CHA structure, and no new crystalline phase was detected. The crystalline size of the Cu-SSZ-13, P_1Cu and P_2Cu are 396 nm, 389 nm, and 392 nm, respectively, obtained with the XRD data using the Scherrer Equation, shown in Table 2. This is consistent with the SEM results, which shows the samples have a similar

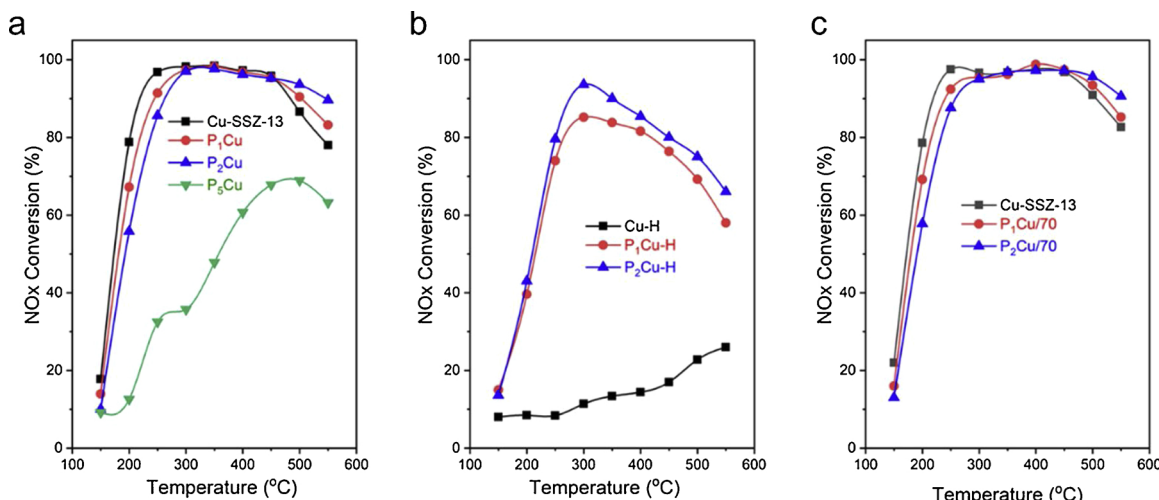


Fig. 1. NO_x conversion during standard NH_3 -SCR as a function of the temperature (150–550 °C) of the (a) fresh (b) Cu-SSZ-13 and P_xCu catalyst samples hydrothermally treated at 750 °C for 16 h and (c) Cu-SSZ-13 and P_xCu catalyst samples hydrothermally treated at 70 °C for 16 h. Reaction conditions: 500 ppm NO, 500 ppm NH_3 , 5% O_2 , 5% H_2O , balanced with N_2 ; flow rate: 500 mL/min, GHSV: 300, 000 h^{-1} .

Table 2

Al, Cu and Si contents and the relative crystallinity of the fresh and aged samples.

Sample	Cu content ^a (wt.%)	Al content ^a wt.%	Si content ^a wt.%	Si/Al ratio ^b	Crystalline size ^c (nm)	Relative crystallinity ^d 100%
Cu-SSZ-13	4.92	9.97	43.5	4.36	396	100
P ₁ Cu	4.91	10.2	43.5	4.25	389	92
P ₂ Cu	4.92	10.4	42.9	4.14	392	84
Cu-H	4.89	9.80	42.8	4.20	＼	0
P ₁ Cu-H	4.95	9.90	43.2	4.20	＼	52
P ₂ Cu-H	4.93	9.90	43.3	4.19	＼	68

a, Determined with the ICP.

b, The mole ratio of the Si/Al determined with the ICP results.

c, The crystalline size was obtained with the XRD data using the Scherrer Equation.

d. Assuming crystallinity of the Cu-SSZ-13 sample to be 100% and the relative crystallinity of the other samples after acid or hydrothermal aging treatment calculated with the following equation:

$$\text{Relative crystallinity (\%)} = \left(\frac{\text{sum of the intensities of the peaks at } 2\theta = 9.4, 20.5 \text{ and } 30.4 \text{ after treatment}}{\text{sum of the intensities of the peaks at } 2\theta = 9.4, 20.5 \text{ and } 30.4 \text{ before treatment}} \right) \times 100\%$$

Table 3Surface areas and pore volumes acid amounts of Cu-SSZ-13 and P_xCu catalysts before and after hydrothermal aging.

Sample	Micropore surface area ^a (m ² /g)	External surface area ^a (m ² /g)	Surface Area ^a (m ² /g)	Pore volume ^b (cm ³ /g)
Cu-SSZ-13	400	5	405	0.20
P ₁ Cu	382	2	383	0.19
P ₂ Cu	351	2	353	0.17
Cu-H	4	4	8	0.00
P ₁ Cu-H	259	9	265	0.14
P ₂ Cu-H	270	6	276	0.15

a. Calculated using BET equation.

b. Determined using the t-plot method.

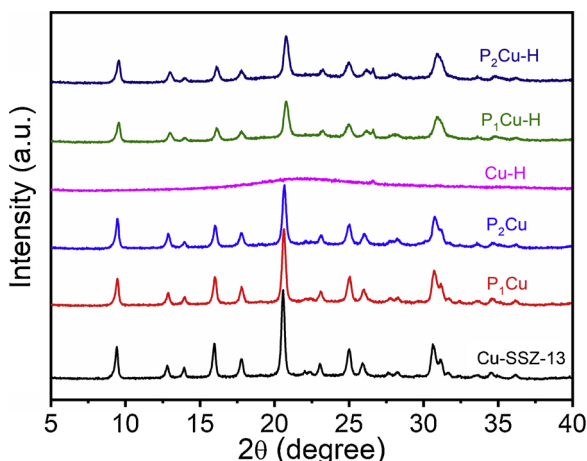


Fig. 2. XRD patterns of the fresh and aged catalysts.

mean crystallite size of around 400 nm, shown in Fig. S4. The XRD intensities slightly decreased with the incorporation of phosphorus on the catalysts P₁Cu and P₂Cu, as compared to the as-prepared Cu-SSZ-13. Data in Table 2 show the relative crystallinity decreased with the increase of the phosphorus content. This reveals minor destruction of the crystalline structure caused by the phosphorus incorporation.

All the signature peaks of Cu-SSZ-13 disappeared after the hydrothermal aging (Cu-H), as shown in Fig. 2, indicating the complete collapse of the crystalline structure. Nevertheless, the typical CHA structure was still retained with the phosphorus incorporation after the hydrothermal aging, and 52% and 68% of the relative crystallinity remained for the P₁Cu-H and P₂Cu-H, respectively, as shown by the data in Table 2.

3.2.2. ³¹P MAS NMR

In Fig. 3a, no phosphorous species were found in the as-prepared Cu-SSZ-13 according to the ³¹P MAS NMR spectra, whereas a broad resonance peak was observed from 0 to -60 ppm with the phosphorus loaded catalysts. The resonance peak can be deconvoluted into four at around -6 ppm, -12 ppm, -32 ppm and -46 ppm, respectively. The assignments for the peaks around -6 ppm, -12 ppm and -46 ppm have been studied intensively, which are the phosphorus atoms in pyrophosphoric species [41,42], phosphorous in less-condensed polyphosphates such as polyphosphates or certain specially polymerized short-chain polyphosphates [43], and phosphorous in branching groups in condensed polyphosphates such as P₄O₁₀ [41,43], respectively.

The assignment of the dominant broad peak centered at -32 ppm is relatively difficult. Similar resonance has been reported with phosphorus modified ZSM-5, and assigned to either phosphate species bonded with extra-framework aluminum or phosphate species connected with the framework aluminum [36,42,44]. Here, it is plausible to give a similar assignment for the broad resonance with the Cu-SSZ-13 samples, to phosphate species bonded with Al either in the framework or in the extra-framework. This will be further discussed in Section 4.2.

As shown in Fig. 3b and Table 4, the shape of the ³¹P MAS NMR spectra narrowed with the hydrothermal aging on the P_xCu-H samples, caused by the decrease of the low-field signals (-6 and -12 ppm) and the increase of the broad signal centered at around -32 ppm. Note that the increased ratio of the phosphate species showing resonances at -32 ppm is equivalent to the decline of pyrophosphoric species (-6 ppm) and less-condensed polyphosphates (-12 ppm) as shown in Table 4, suggesting the transformation between the different phosphate species during hydrothermal aging.

3.2.3. ²⁷Al MAS NMR

²⁷Al MAS NMR is sensitive to the coordination of Al atoms in zeolites. As shown in Fig. 4a, the ²⁷Al MAS NMR spectra of Cu-SSZ-13 and P_xCu samples show a strong peak at around 56 ppm, assigned to the tetrahedral framework Al (TFAI) species in the zeolite framework [4,9]. Meanwhile, a new peak at around 0 ppm appeared with the phosphorus loading on Cu-SSZ-13, assigned to the octahedral extra-framework Al (EFAI) in the phosphorus modified samples [22]. The relative contribution of the respective Al species is shown in Table 5. Around 94% and 86% TFAI remained in the P₁Cu and P₂Cu, respectively, using the integrated peak area at around 56 ppm in the as-prepared Cu-SSZ-13 as a reference, shown in Table 5 [4,24]. Nevertheless, only around 3% of Al converted to EFAI in both the phosphorus-modified samples, indicating a part of Al was undetectable with the ²⁷Al MAS NMR.

A significant change was observed in the ²⁷Al MAS NMR spectra after the hydrothermal treatment, as shown in Fig. 4b. The intensity of the TFAI peak centered at 56 ppm almost vanished over the sample Cu-

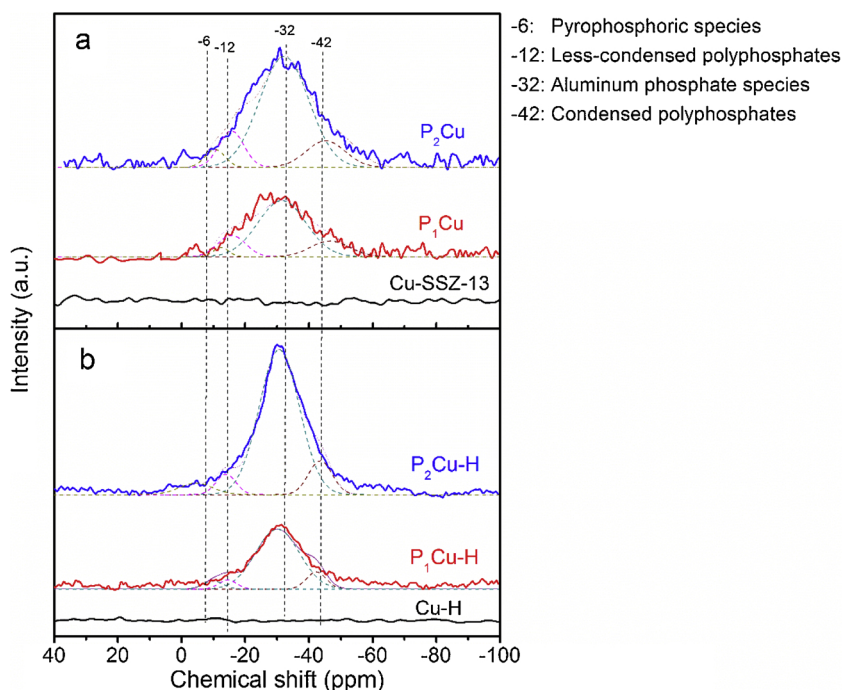


Fig. 3. Solid state ^{31}P MAS NMR spectra of the (a) fresh and (b) aged Cu-SSZ-13 and P_xCu samples. The original ^{31}P MAS NMR profiles are represented with the solid lines. The fitted peaks are represented as dash lines and highlighted with different colours (wine, dark cyan, magenta and dark yellow) for comparison. The assignment of the resonance peaks is presented in the right part of the figure (For interpretation of the references to colour in this figure legend, the reader is referred to the web version of this article).

H. Meanwhile, the decrease of the TFAI signal intensity with the P-loaded sample indicates significant degradation after the hydrothermal treatment, whereas about 48% and 57% of the TFAI species still remained in the $\text{P}_1\text{Cu-H}$ and $\text{P}_2\text{Cu-H}$ samples, respectively (Table 5).

Interestingly, a new peak at 39 ppm exclusively appeared after the hydrothermal aging with the phosphorus-doped catalysts. According to previous works [24,45], the peak at 30 ppm was clearly assigned to the penta-coordinated Al for Al in SSZ zeolite. As is known, the chemical shift of ^{27}Al nuclear moves to a lower position with the increasing number of ligands, which was caused by the increased shielding effect [46,47]. Therefore, pentahedral framework Al with more ligands than the distorted tetrahedral framework Al should show a lower chemical shift. Along this line, the signal of 39 ppm is likely ascribed to the distorted TFAI, consistent with previous works of P modified Y and ZSM-5 [36,43,48,49].

3.2.4. Raman

Raman spectra were used to verify the structural changes of the phosphate and aluminate entities in the samples, as shown in Fig. 5. The Raman band at around 1076 cm^{-1} with the P_xCu samples was observed in the P doped samples. This may be ascribed to $\text{P}(\text{OH})_3$ or the stretching vibrations of P-O-Al bonds in amorphous aluminophosphate species [50,51]. The ^{31}P MAS NMR measurement in Fig. 3 rules out the

existence of the $\text{P}(\text{OH})_3$ in the P doped samples. Therefore, the band at 1076 cm^{-1} indicates the amorphous aluminophosphate exist in the fresh P doped samples. After hydrothermal treatment, the band at around 1076 cm^{-1} with the P_xCu samples upshifted to 1100 cm^{-1} , as shown in Fig. 5. This can be explained by the emergence of the phosphorus-oxygen tetrahedron coordinated with the lattice Al^{3+} in the tetrahedral sites in the phosphorus loaded samples during the hydrothermal treatment [52,53].

3.3. Effect of phosphorus on the cupric species

3.3.1. EPR

Figs. 6 and 7 present EPR results of the fresh and the aged samples, respectively. The hyperfine structures of the EPR spectra were resolved and enlarged in the inset for the fresh and the aged samples. $g_{//} = 2.39$ and $A_{//} = 131\text{ G}$ were observed with all the fresh samples as well as the $\text{P}_x\text{Cu-H}$ samples, ascribed to the octahedral coordination of isolated Cu^{2+} ions [54,55]. Meanwhile, $g_{//} = 2.32$ and $A_{//} = 155\text{ G}$ was observed in the sample Cu-H, corresponding to the Cu^{2+} ions on Al_2O_3 [23]. This indicates the change of the Cu^{2+} coordination in the undoped sample in the hydrothermal aging treatment.

The relative amount of Cu^{2+} ions in the samples were normalized using the isolated Cu^{2+} ions content in Cu-SSZ-13 as a reference, as

Table 4
Relative phosphate distribution observed with ^{31}P MAS NMR for fresh and aged Cu-SSZ-13 and P_xCu samples

Sample	P atoms (%) ^a	–42 ppm Condensed polyphosphates	–32 ppm Aluminum phosphate	–12 ppm Less-condensed polyphosphates	–6 ppm Pyrophosphoric species	Changed ratio
Cu-SSZ-13	ND ^b		ND	ND	ND	
P_1Cu	14.1		66.5	13.6	5.8	
P_2Cu	13.9		67.3	11.9	6.9	
Cu-H	ND		ND	ND	ND	
$\text{P}_1\text{Cu-H}$	14.1		75.5	5.2	5.1	9.1 ^c /9.0 ^d
$\text{P}_2\text{Cu-H}$	13.6		76.1	5.4	4.9	8.5/8.8

a. The distribution of different phosphorous species based on the deconvolution of the ^{31}P MAS NMR results.

b. ND denotes not detected.

c. The decreased ratio of the less-condensed polyphosphates and pyrophosphoric species after hydrothermal treatment.

d. The increased ratio of the aluminum phosphate species after hydrothermal treatment.

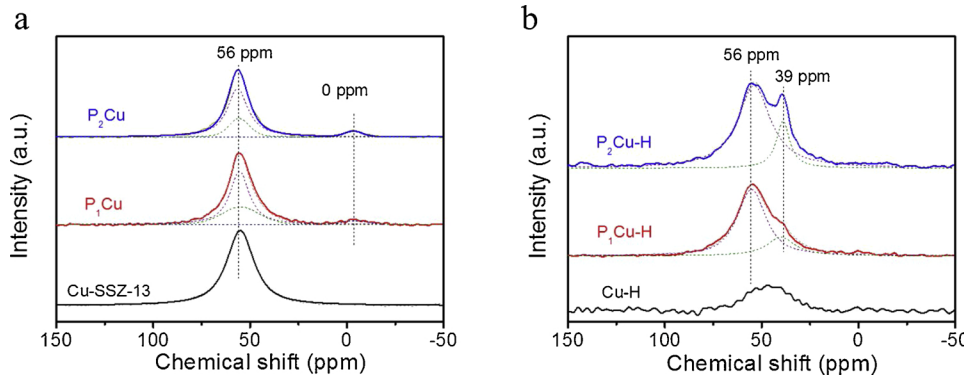


Fig. 4. Solid state ^{27}Al MAS NMR spectra of the (a) fresh and (b) aged Cu-SSZ-13 and PxCu samples. The solid lines represent the original ^{27}Al MAS NMR profiles. The fitted peak at 0 ppm highlighted with green dash line, and the green dash line represents the fitted peak at 39 ppm. The navy and olive dash lines stand for the fitted peak at 56 ppm. The sum of all fitted peak is shown as a gray dash line. (For interpretation of the references to colour in this figure legend, the reader is referred to the web version of this article).

Table 5

Relative Al contribution of the TFAI, EFAI, distorted TFAI and undetected Al species observed with ^{27}Al MAS NMR for catalyst samples.

Sample	Al distribution (100%)			
	TFAI ^a (56 ppm)	EFAI ^a (0 ppm)	Distorted TFAI ^a (39 ppm)	Undetected Al ^b
Cu-SSZ-13	100	0	0	0
P ₁ Cu	94	1	0	5
P ₂ Cu	86	3	0	11
P ₁ Cu-H	48	0	10	42
P ₂ Cu-H	57	0	17	26

a. Assuming the ^{27}Al MAS NMR resonance peak area in the Cu-SSZ-13 sample to be 100% and the relative contributions of the respective Al species in the samples according to the deconvolution result of NMR spectra.

b. The percentage of the Al species undetected with the ^{27}Al MAS NMR measurement, calculated with the one hundred percentage subtract the contribution of the TFAI, EFAI and distorted TFAI.

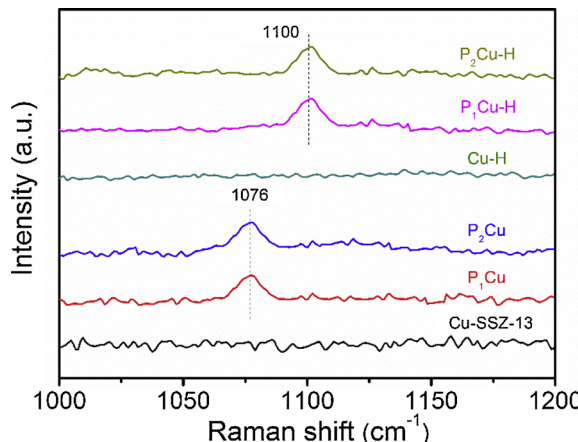


Fig. 5. The Raman shift at around 1100 cm^{-1} of the fresh and aged catalysts.

shown in Fig. 8. The amount of isolated Cu^{2+} ions decreased by around 18% in P_1Cu sample and by around 35% for P_2Cu sample, respectively, as compared to the Cu-SSZ-13 without P. After hydrothermal treatment, almost all the isolated Cu^{2+} ions vanished in the Cu-H sample. Nevertheless, about 45% and 53% of isolated Cu^{2+} ions still remained in the $\text{P}_1\text{Cu-H}$ and the $\text{P}_2\text{Cu-H}$ samples, respectively, as compared to the Cu-SSZ-13.

3.3.2. H_2 -TPR

Fig. 9 shows the H_2 -TPR plots with the fresh and the hydrothermally aged samples. Two peaks were recorded with the Cu-SSZ-13 in Fig. 9a, caused by H_2 consumption of Cu^{2+} reduced to Cu^+ below 450°C , and Cu^+ reduced to Cu° above 600°C , respectively, as shown in Eq. (5) and

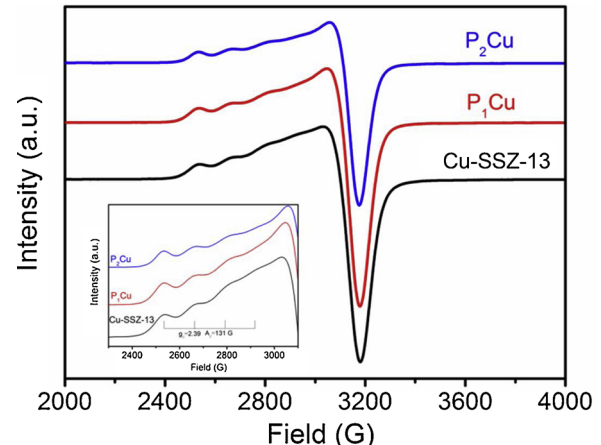


Fig. 6. Electron Paramagnetic Resonance (EPR) spectra of the fresh catalyst samples. The insert displays hyperfine features of the EPR spectra for the samples. Spectra were collected at -150°C . $g// = 2.39$ and $A// = 131\text{ G}$ was ascribed to the octahedral coordination of isolated Cu^{2+} ions [54].

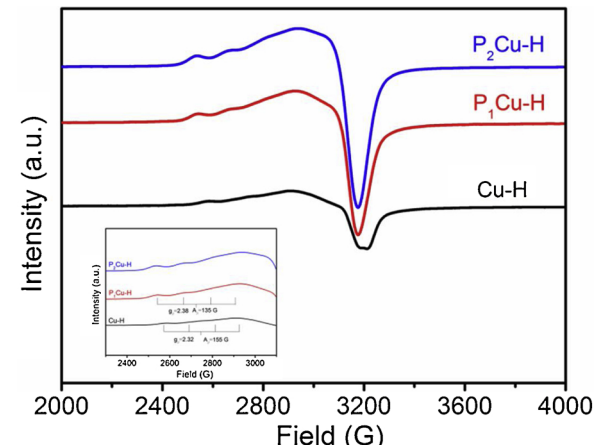


Fig. 7. Electron Paramagnetic Resonance (EPR) spectra of the aged catalyst samples. The insert displays hyperfine features of the EPR spectra for the samples. Spectra were collected at -150°C . $g// = 2.39$ and $A// = 131\text{ G}$ was ascribed to the octahedral coordination of isolated Cu^{2+} ions [30,43], and $g// = 2.32$ and $A// = 155\text{ G}$ can be attributed to the Cu^{2+} ions on Al_2O_3 [23].

(6) [3,9,51,54,56].



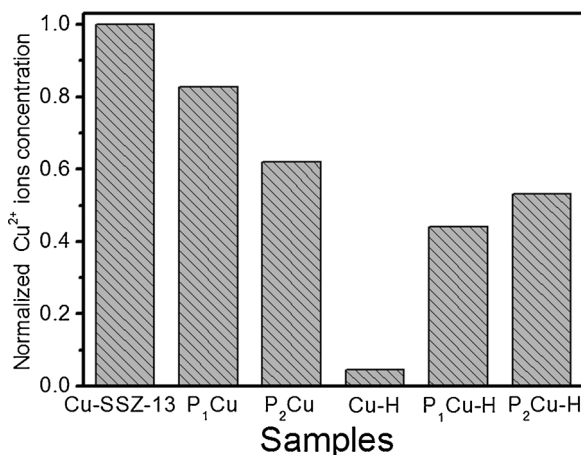


Fig. 8. The normalized Cu²⁺ ions concentration determined with double integrating the EPR spectra using the Cu-SSZ-13 as a reference.

Note that more reduction of Cu²⁺ to Cu⁺ than the Cu⁺ to Cu⁰ was observed in the fresh samples, which can be ascribed to the reduction of a part of Cu⁺ ions occurs at the temperature higher than 800 °C. This is consistent with the previous work by Xie et al. [9], in which the Cu-SSZ-13 synthesized with the one-pot method shows a H₂-reduction peak of Cu⁺ at around 900 °C.

The peak from 250 to 400 °C with the Cu-SSZ-13 sample was deconvoluted into two peaks around 280 °C and 335 °C, respectively. The peak at around 280 °C is assigned to the reduction of [Cu(OH)]⁺ near the eight-membered ring (8MR), whereas the peak at around 335 °C is attributed to the reduction of the naked Cu²⁺ ions coordinated to the paired Al in 6MR (Cu²⁺-2Al) [17,22,57]. The intensity of the peak at around 280 °C decreased with the increase of phosphorus doping content in the P_xCu sample, indicating the amount of isolated Cu²⁺ ions decreased as compared to the Cu-SSZ-13.

An H₂ consumption peak at around 535 °C emerged in the P_xCu samples, much higher than the reduction temperature of isolated Cu²⁺ ions (below 400 °C). Probably, this new peak may be ascribed to the reduction of some newly formed Cu-phosphate species with lower redox capacity than the isolated Cu²⁺ ions [9,54,56]. However, we have no further evidence on determining the exact state of the Cu-phosphate, since different phosphate species exist in the P doped samples according to the ³¹P MAS NMR results in Fig. 3.

The H₂-TPR plots of the hydrothermally aged samples are shown in Fig. 9b. For the sample Cu-H, the reduction peaks appeared at around 230 °C and 260 °C should be ascribed to the reduction of Cu²⁺ on Al₂O₃, according to the EPR results in Fig. 7. The H₂ consumption peak at above 600 °C remained with the two P_xCu-H samples, indicating that they still contain a large amount of the isolated Cu²⁺ ions. Meanwhile, a broad peak is shown between 180 °C and 400 °C with the P_xCu-H samples which can be deconvoluted into two peaks, at around 200 °C and 290 °C, respectively. The peak around 200 °C can be assigned to the

reduction of aggregated CuO_x, because a reduction peak at similar temperature was observed with CuO powder as a reference in Fig. S6. Another peak around 290 °C appeared exclusively with the samples with phosphorous, attributed to the reduction of the remaining isolated Cu²⁺ ions. Only one reduction peak of isolated Cu²⁺ ions was observed in the aged P doped samples. This can be ascribed to the overlap of the reduction profiles of the [Cu(OH)]²⁺ and Cu²⁺-2Al or the transformation between Cu(OH)⁺ and Cu²⁺-2Al during hydrothermal treatment [28,58].

4. Discussion

4.1. Hydrothermal aging effect on the structure

The hydrothermal aging at 750 °C for 16 h destroyed the Cu-SSZ-13 structure completely for the sample without P loading (the sample Cu-H), according to the XRD pattern in Fig. 2a. The surface area and the pore volume of the sample lost almost completely as shown in Table 3.

It has been well documented that Brønsted acid sites (i.e., -Si-(OH)-Al-) in zeolites are the most vulnerable to H₂O attack during hydrothermal aging, resulting in the collapse of the zeolite structure with dealumination [45]. The mechanism of the dealumination is summarized in Scheme 1. First, the framework acidic Si-(OH)-Al sites can be easily hydrolyzed, forming a vicinal disilanol defect as well as a new Brønsted acid site in the vicinity, as shown in Step 1 in Scheme 1 [31,59]. In Step 2, the formation of vicinal disilanol defect results in weakening and cleavage of the Al-O bonding [31,60]. Subsequently, as shown in step 3, the hydroxylation of Si-(OH)-Al framework continuously repeats the two steps above mentioned, eventually resulting in complete expulsion of the Al from the framework, causing the collapse of the structure [19,60]. The mechanism is confirmed with NH₃-TPD in this work, where almost no NH₃ desorption was observed with Cu-H (Fig. S5), indicating the complete disappearance of Si-(OH)-Al sites. Furthermore, ²⁷Al MAS NMR with the Cu-H sample in Fig. 4b shows the peak at around 56 ppm decreased significantly, suggesting the vanishing of the TFAI via dealumination.

4.2. Phosphorus effect on the structure

4.2.1. Phosphorus effect before aging

The XRD in Fig. 2a and the data in Table 2 show minor structural destruction in the phosphorus loaded samples. Meanwhile, the as-prepared Cu-SSZ-13 contains only TFAI, whereas the EFAI emerged in the P_xCu samples without hydrothermal treatment, according to ²⁷Al MAS NMR in Fig. 4a. This indicates partial detachment of the TFAI from the framework. These observations suggest that the detachment of partial TFAI contributes to the structure destruction of the P_xCu samples.

The total Al content remained constant as confirmed with the ICP data in Table 2. Nevertheless, around 10% Al was undetectable via ²⁷Al MAS NMR with the P_xCu samples shown in Table 5. This can be explained by the well-accepted theory that certain content of Al species was beyond the detection in the ²⁷Al MAS NMR due to the second-order

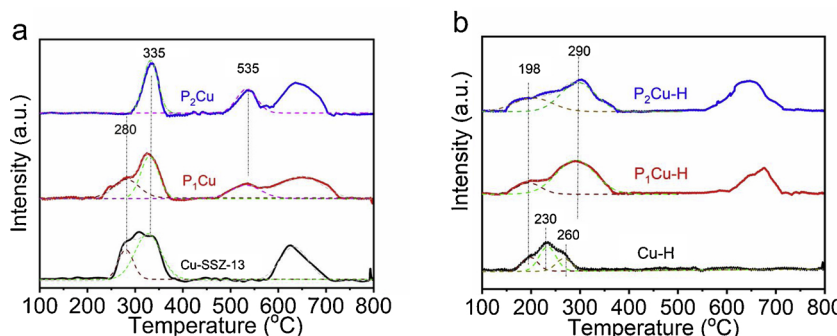
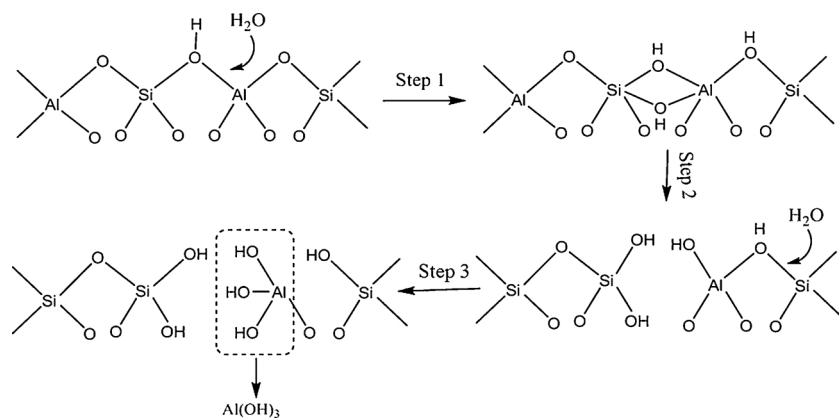


Fig. 9. H₂-TPR spectra of (a) fresh and (b) aged samples. The fitted peak at 280 °C highlighted with purple dash line, and the green line represents the fitted peak at 335 °C. For the aged samples, the fitted peaks with tops at 200 °C, 250 °C, 535 °C and 290 °C are highlighted (orange, pink, wine and olive) for comparison. The violet dash line stands for the fitted peak above 600 °C. The sum of all fitted peak is shown as a gray dash line (For interpretation of the references to colour in this figure legend, the reader is referred to the web version of this article).



Scheme 1. SSZ-13 zeolite hydrolysis process.

quadrupolar interactions in the Al nucleus [49,61,62]. The formation of highly distorted Al species and the paramagnetic Cu^{2+} species situated next to extra-framework Al can cause the "NMR invisible Al" in ^{27}Al MAS NMR spectra [4,24].

The ^{31}P MAS NMR (Fig. 3a) and Raman (Fig. 5) spectra corroborate that the aluminum phosphate species exists in the P_xCu samples [36,42,44], while no such Al species was observed in the ^{27}Al MAS NMR results (Fig. 4a). This clearly confirms that Al interacting with the phosphate caused a part of the Al species highly distorted, undetectable in ^{27}Al MAS NMR with the P_xCu samples. No line broadening of the TFAI signal was observed in ^{27}Al MAS NMR in Fig. 4a, ruling out the interaction between phosphate and the framework Al in the P_xCu samples [58]. Therefore, the undetectable Al can be ascribed to the extra-framework aluminum phosphates formed with part of the EFAl interacting with the phosphate, agreeing with the previous results with phosphorus modified Y and ZSM-5 [44,63,64]. However, the impact of the paramagnetic Cu^{2+} species on the measurement of extra-framework Al in ^{27}Al MAS NMR is unavoidable [4]. Accordingly, we cannot discard the possibility that a part of invisible Al was caused by the influence paramagnetic Cu species in the ^{27}Al MAS NMR measurement.

4.2.2. Improvement of skeleton stability

The crystalline structure, as well as over 65% of the surface area and pore volume, retained with the $\text{P}_x\text{Cu}-\text{H}$ samples after the hydrothermal treatment, according to XRD (Fig. 2 and Table 2) and N_2 physisorption measurement (Table 3) data, significantly improved over the $\text{Cu}-\text{H}$ sample without P loading. Moreover, the ^{27}Al MAS NMR results in Table 5 demonstrate that around 50% of TFAI still remained in the aged phosphorus doped samples. In contrast, almost no TFAI retained in the $\text{Cu}-\text{H}$ sample (Table 5). This clearly proves the stabilization effect of the phosphorus species on the Cu-SSZ-13 structure against dealumination during the hydrothermal aging.

The coordination environment of the Al and P changed in the $\text{P}_x\text{Cu}-\text{H}$ samples after the hydrothermal treatment, if compared to that in the fresh samples. As shown in Fig. 4b and Table 5, the distorted TFAI species appeared in the $\text{P}_x\text{Cu}-\text{H}$ samples, increasing with the increase of the phosphorus amount according to ^{27}Al MAS NMR (Table 5). Meanwhile, the pyrophosphoric species (-6 ppm) and less-condensed polyphosphates (-12 ppm) transferred to aluminum phosphate species (-32 ppm) during the hydrothermal aging according to ^{31}P MAS NMR in Fig. 3b and Table 4. There seems to exist a correlation between the formation of distorted TFAI and the transformation of the phosphate species. This is confirmed by the shift of the peak assigned to the P-O-Al lattice vibration with phosphorus modified samples according to the Raman spectra in Fig. 5 [52,53]. Additionally, no crystalline AlPO_4 phase was observed via XRD in Fig. 2, ruling out any crystallization of the extra-framework aluminum phosphates [51,52]. As a result, the shift of the Raman peak indicates the formation of distorted TFAI

coordinating with the phosphate species, resulting in a framework silicoaluminophosphate interface, as shown in Scheme 2.

The interaction between the distorted TFAI and the phosphate species probably caused by the well-known fact that the positively charged $[\text{PO}_4]^{3-}$ in the phosphate can neutralize the negatively charged $[\text{AlO}_4]^{-}$ containing TFAI in the zeolite lattice, eliminating the Brønsted acidity as well as the ability to dissociate water, as shown in Scheme 2 [36,63]. This prevents degradation of the distorted TFAI with further breakage of the residual Si-O-Al bond under hydrothermal condition (Step 3, Scheme 1).

Around 7% higher amount of TFAI and distorted TFAI species retained in the $\text{P}_2\text{Cu}-\text{H}$ sample as compared to that in the $\text{P}_1\text{Cu}-\text{H}$ sample according to the ^{27}Al MAS NMR results (Table 5). This indicates the distorted TFAI species protects other TFAI against dealumination during hydrothermal treatment, thus keeping the long-range order of structure stable, as confirmed with the XRD results in Fig. 2. This proposal was shown in Scheme 3.

4.3. Effect on the Cu species

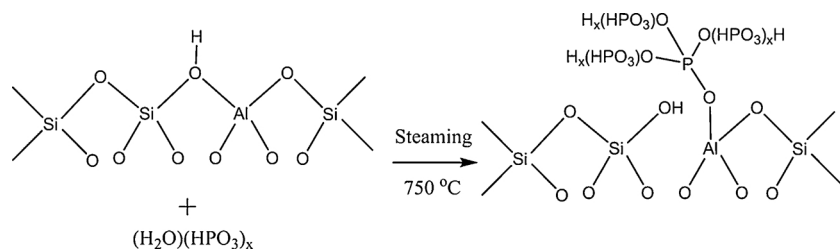
4.3.1. In the fresh samples

The isolated Cu^{2+} ions amount decreased with increasing phosphate content, according to the EPR result in Fig. 8. No CuO_x appeared in the P_xCu samples according to the H_2 -TPR results (Fig. 9a), ruling out the agglomeration of the isolated Cu^{2+} ions to CuO_x caused by dealumination [19]. Therefore, the decline of the isolated Cu^{2+} ion content can be attributed to the formation of Cu-phosphates in the phosphorus-doped samples as shown in Fig. 9a, consistent with the previous work [65].

4.3.2. In the aged samples

Only Cu^{2+} ions on Al_2O_3 were observed in the $\text{Cu}-\text{H}$ sample after the hydrothermal aging, according to the EPR results in Fig. 7. Nevertheless, no such species was detected with ^{27}Al MAS NMR, as shown in Fig. 4b no signal at 0 ppm which represents octahedral Al. This is ascribed to the interaction of the paramagnetic Cu^{2+} ions with the quadrupolar ^{27}Al nuclei which makes the octahedral aluminum "NMR invisible", as discussed in Section 4.2.1. [4,24].

A large amount of isolated Cu^{2+} ions remained in the $\text{P}_x\text{Cu}-\text{H}$ samples according to the EPR results in Fig. 8. Furthermore, both the content of the isolated Cu^{2+} ions as well as the TFAI increased with the increase of the phosphorus loading in the aged samples, according to Fig. 8 and Table 5. The cupric species have been known prefer to stay as isolated Cu^{2+} coordinating to the TFAI to maintain low free energy if the structure remains intact in the hydrothermal treatment [26,28]. Therefore, the phosphorus protects the isolated Cu^{2+} ions by retaining the TFAI in the framework during the hydrothermal treatment.



Scheme 2. The phosphorus stabilization effect on the phosphorus modified samples ($x = 0, 1, 2, \dots$).

4.4. Effect on the SCR performance

4.4.1. Before hydrothermal aging

The P_xCu sample exhibited a decline of SCR activity below 250 °C, as compared to those of the Cu-SSZ-13, as shown in Fig. 1a. This is probably caused by the high redox barriers for the Cu-phosphate species according to H₂-TPR in Fig. 9, making it inactive for SCR reaction, which is known as highly dependent on the redox of cupric sites in Cu-SSZ-13 [66,67].

The NO_x conversions with the P_xCu samples are higher than the Cu-SSZ-13 with reaction temperature higher than 450 °C, as shown in Fig. 1a. It is known that NH₃ oxidation rate increased at such high temperature, as a competitive reaction with NH₃-SCR [68]. Fig. 8 shows lower isolated Cu²⁺ content in the P_xCu samples than in the Cu-SSZ-13. Probably, NH₃ oxidation is dependent on the isolated Cu²⁺ content than NH₃-SCR, resulting in a decline of the reaction rate for NH₃ oxidation and less consumption of NH₃, promoting the NH₃-SCR reaction rate by more reactant [68,69]. This agrees with the decline of NH₃ conversion with the phosphorus doped samples in NH₃ oxidation experiments, as shown in Fig. S7a in the *Supporting Information*.

4.4.2. After hydrothermal aging

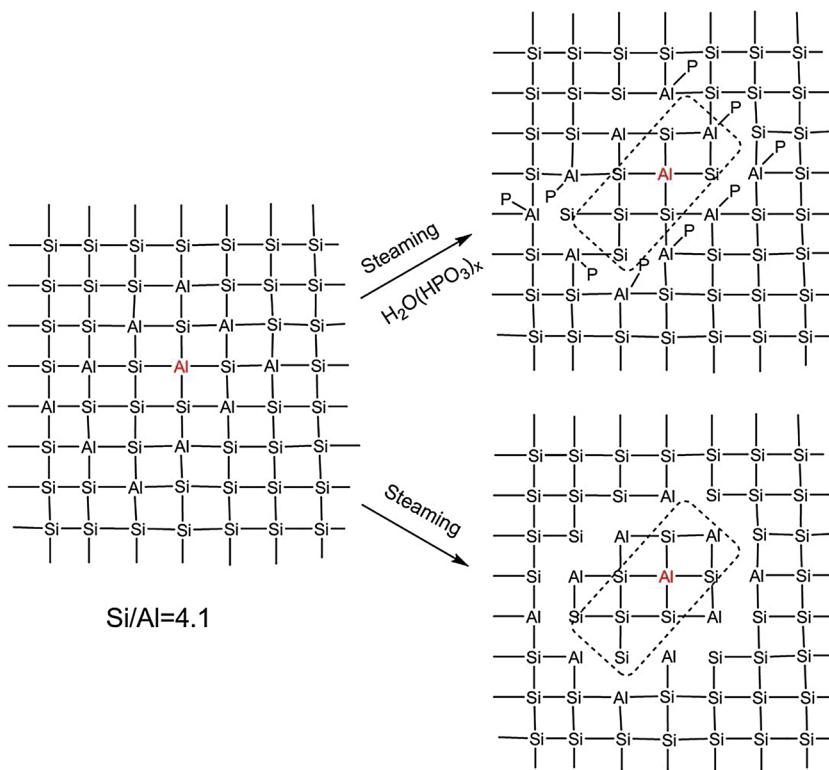
As shown in Fig. 1b, the NO_x conversion with the non-phosphorus doped sample (Cu-H) decreased significantly after the hydrothermal aging at 750 °C, as compared with the Cu-SSZ-13 before hydrothermal

aging in Fig. 1a. The phosphorus doping increased the NO_x conversion significantly from 150 °C to 550 °C (P₁Cu-H and P₂Cu-H) as shown in Fig. 1b. This can be explained by the stabilization effect of the phosphate ions interacting with the framework, as well as the remaining of the isolated Cu²⁺ ions, as discussed in Section 4.2 and 4.3. Notably, the catalyst with the high phosphorus content (P₂Cu-H) shows the best activity. The excellent activity above 450 °C can be explained by less competition of NH₃ oxidation at the temperatures (Fig. S7b), similar to the sample before hydrothermal aging as discussed in Section 4.4.1.

5. Conclusion

Doping with P as phosphate acid detach a part of TFAI to EFAl in the Cu-SSZ-13. Nevertheless, the formation of a framework silicoaluminophosphate interface retards the further dealumination of the Cu-SSZ-13 sample with phosphorus doping, retaining the CHA structure intact.

For the cupric sites, the isolated Cu²⁺ ions react partly with the phosphate, forming the Cu-phosphate species in the P_xCu samples. The Cu-phosphate species may be inactive for NH₃-SCR reaction due to the very high redox barriers (H₂-reduction temperature at around 535 °C) of the cupric species. This reduces the SCR performance of P_xCu samples at low temperatures, whereas enhancing their deNO_x activity above 450 °C. After hydrothermal treatment, the isolated Cu²⁺ ions vanished due to the structural collapse. In contrast, the intact structure of the aged samples with P loading retains most of the isolated Cu²⁺



Scheme 3. The possible mechanism of phosphorus protection effect on the structure of the phosphorus-doped samples; (a) the interlinkage of framework Si and Al in the framework; (b) the protection effect of the distorted TFAI on the network of the P_xCu -H catalysts; (c) the detachment of the framework Al in the sample without phosphorus.

ions, maintaining their excellent SCR performance.

A small amount of P (around 1–2 wt.%) in the tail gas may be favorable for the hydrothermal stability of Cu-SSZ-13 with a low Si/Al ratio. However, the high P content (around 5 wt.%) seriously decrease the deNO_x activity of the doped sample. Therefore, the amount of P in the vehicle exhaust should be precisely controlled.

Acknowledgments

This work was supported in part by the Program of Introducing Talents to the University Disciplines under file number B06006, and the Program for Changjiang Scholars and Innovative Research Teams in Universities under file number IRT 0641.

Appendix A. Supplementary data

Supplementary material related to this article can be found, in the online version, at doi:<https://doi.org/10.1016/j.apcatb.2019.04.037>.

References

- [1] I. Nova, E. Tronconi, *Urea-SCR Technology for deNO_x After Treatment of Diesel Exhausts*, Springer, New York, 2014.
- [2] J. Wang, H. Chen, Z. Hu, M. Yao, Y. Li, *Catal. Rev.* 57 (2014) 79–144.
- [3] H. Zhao, H. Li, X. Li, M. Liu, Y. Li, *Catal. Today* 297 (2017) 84–91.
- [4] J.H. Kwak, D. Tran, S.D. Burton, J. Szanyi, J.H. Lee, C.H.F. Peden, *J. Catal.* 287 (2012) 203–209.
- [5] G. Liu, P.-X. Gao, *Catal. Sci. Technol.* 1 (2011) 552.
- [6] X. Dong, J. Wang, H. Zhao, Y. Li, *Catal. Today* 258 (Part 1) (2015) 28–34.
- [7] G. Cavataio, H.-W. Jen, J.W. Girard, D. Dobson, J.R. Warner, C.K. Lambert, *SAE Int. J. Fuels Lubr.* 2 (2009) 204–216.
- [8] X. Chen, N. Currier, A. Yezersets, K. Kamasamudram, *SAE Int. J. Eng.* 6 (2013) 856–861.
- [9] L. Xie, F. Liu, X. Shi, F.-S. Xiao, H. He, *Appl. Catal. B: Environ.* 179 (2015) 206–212.
- [10] J.H. Kwak, R.G. Tonkyn, D.H. Kim, J. Szanyi, C.H.F. Peden, *J. Catal.* 275 (2010) 187–190.
- [11] D.W. Fickel, E. D'Addio, J.A. Lauterbach, R.F. Lobo, *Appl. Catal. B: Environ.* 102 (2011) 441–448.
- [12] Y. Shan, X. Shi, J. Du, Y. Yu, H. He, *Catal. Sci. Technol.* 9 (2019) 106–115.
- [13] Y. Shan, X. Shi, Z. Yan, J. Liu, Y. Yu, H. He, *Catal. Today* 320 (2019) 84–90.
- [14] U. Deka, I. Lezcano-Gonzalez, B.M. Weckhuysen, A.M. Beale, *ACS Catal.* 3 (2013) 413–427.
- [15] Y. Zhao, J. Hu, L. Hua, S. Shuai, J. Wang, *Ind. Eng. Chem. Prod. Res. Dev.* 50 (2011) 11863–11871.
- [16] L. Ma, Y. Cheng, G. Cavataio, R.W. McCabe, L. Fu, J. Li, *Appl. Catal. B: Environ.* 156–157 (2014) 428–437.
- [17] J. Wang, H. Zhao, G. Haller, Y. Li, *Appl. Catal. B: Environ.* 202 (2017) 346–354.
- [18] L. Ma, Y. Cheng, G. Cavataio, R.W. McCabe, L. Fu, J. Li, *Chem. Eng. J.* 225 (2013) 323–330.
- [19] D. Wang, Y. Jangjou, Y. Liu, M.K. Sharma, J. Luo, J. Li, K. Kamasamudram, W.S. Epling, *Appl. Catal. B: Environ.* 165 (2015) 438–445.
- [20] A.M. Beale, F. Gao, I. Lezcano-Gonzalez, C.H.F. Peden, J. Szanyi, *Chem. Soc. Rev.* 44 (2015) 7371–7405.
- [21] F. Gao, J.H. Kwak, J. Szanyi, C.H.F. Peden, *Top. Catal.* 56 (2013) 1441–1459.
- [22] F. Gao, N.M. Washton, Y. Wang, M. Kollár, J. Szanyi, C.H.F. Peden, *J. Catal.* 331 (2015) 25–38.
- [23] Y.J. Kim, J.K. Lee, K.M. Min, S.B. Hong, I.-S. Nam, B.K. Cho, *J. Catal.* 311 (2014) 447–457.
- [24] S. Prodinger, M.A. Derewinski, Y. Wang, N.M. Washton, E.D. Walter, J. Szanyi, F. Gao, Y. Wang, C.H.F. Peden, *Appl. Catal. B* 201 (2017) 461–469.
- [25] J.R. Di Iorio, R. Gounder, *Chem. Mater.* 28 (2016) 2236–2247.
- [26] C. Paolucci, A.A. Parekh, I. Khurana, J.R. Di Iorio, H. Li, J.D. Albarracin Caballero, A.J. Shih, T. Anggara, W.N. Delgass, J.T. Miller, F.H. Ribeiro, R. Gounder, W.F. Schneider, *J. Am. Chem. Soc.* 138 (2016) 6028–6048.
- [27] J. Luo, D. Wang, A. Kumar, J. Li, K. Kamasamudram, N. Currier, A. Yezersets, *Catal. Today* 267 (2016) 3–9.
- [28] J. Song, Y. Wang, E.D. Walter, N.M. Washton, D. Mei, L. Kovarik, M.H. Engelhard, S. Prodinger, Y. Wang, C.H.F. Peden, F. Gao, *ACS Catal.* 7 (2017) 8214–8227.
- [29] S. Han, J. Cheng, C. Zheng, Q. Ye, S. Cheng, T. Kang, H. Dai, *Appl. Surf. Sci.* 419 (2017) 382–392.
- [30] Z. Zhao, R. Yu, R. Zhao, C. Shi, H. Gies, F.-S. Xiao, D. De Vos, T. Yokoi, X. Bao, U. Kolb, M. Feyen, R. McGuire, S. Maurer, A. Moini, U. Müller, W. Zhang, *Appl. Catal. B: Environ.* 217 (2017) 421–428.
- [31] S. Malola, S. Svelle, F.L. Bleken, O. Swang, *Angew. Chem. Int. Ed. Engl.* 51 (2012) 652–655.
- [32] P. Li, W. Zhang, X. Han, X. Bao, *Catal. Lett.* 134 (2010) 124–130.
- [33] P. Zeng, Y. Liang, S. Ji, B. Shen, H. Liu, B. Wang, H. Zhao, M. Li, *J. Energy Chem.* 23 (2014) 193–200.
- [34] X. Wang, W. Dai, G. Wu, L. Li, N. Guan, M. Hunger, *Microporous Mesoporous Mater.* 151 (2012) 99–106.
- [35] A. Corma, J. Mengual, P.J. Miguel, *Appl. Catal. A Gen.* 460–461 (2013) 106–115.
- [36] J. Zhuang, D. Ma, G. Yang, Z. Yan, X. Liu, X. Liu, X. Han, X. Bao, P. Xie, Z. Liu, *J. Catal.* 228 (2004) 234–242.
- [37] A. Buchholz, W. Wang, M. Xu, A. Arnold, M. Hunger, *Microporous Mesoporous Mater.* 56 (2002) 267–278.
- [38] L. Ren, L. Zhu, C. Yang, Y. Chen, Q. Sun, H. Zhang, C. Li, F. Nawaz, X. Meng, F.S. Xiao, *Chem. Commun. (Camb.)* 47 (2011) 9789–9791.
- [39] N. Yamanaka, M. Itakura, Y. Kiyozumi, Y. Ide, M. Sadakane, T. Sano, *Microporous Mesoporous Mater.* 158 (2012) 141–147.
- [40] K. Xie, J. Woo, D. Bernin, A. Kumar, K. Kamasamudram, L. Olsson, *Appl. Catal. B: Environ.* 241 (2019) 205–216.
- [41] I. Lezcano-Gonzalez, U. Deka, H.E. van der Bij, P. Paalanen, B. Arstad, B.M. Weckhuysen, A.M. Beale, *Appl. Catal. B: Environ.* 154–155 (2014) 339–349.
- [42] K. Damodaran, J.W. Wierch, S.M. Cabral de Menezes, Y.L. Lam, J. Trebosc, J.P. Amoureux, M. Pruski, *Microporous Mesoporous Mater.* 95 (2006) 296–305.
- [43] N. Xue, X. Chen, L. Nie, X. Guo, W. Ding, Y. Chen, M. Gu, Z. Xie, *J. Catal.* 248 (2007) 20–28.
- [44] G. Lischke, R. Eckelt, H.G. Jerschewitz, B. Parlitz, E. Schreier, W. Stork, B. Zibrowius, G. Öhlmann, *J. Catal.* 132 (1991) 229–243.
- [45] F. Gao, Y. Wang, N.M. Washton, M. Kollár, J. Szanyi, C.H.F. Peden, *ACS Catal.* 5 (2015) 6780–6791.
- [46] A.G. Stepanov, *Basics of Solid-State NMR for Application in Zeolite Science* 4 Elesiver, 2016, pp. 137–188 Chapter.
- [47] B.J. Freude, *Cryst. Res. Technol.* 15 (1981) K36–K38.
- [48] Z. Yan, D. Ma, J. Zhuang, X. Liu, X. Liu, X. Han, X. Bao, F. Chang, L. Xu, Z. Liu, *J. Mol. Catal. A Chem.* 194 (2003) 153–167.
- [49] T. Blasco, A. Corma, J. Martínez-Triguero, *J. Catal.* 237 (2006) 267–277.
- [50] A.M. Beale, M.G. O'Brien, M. Kasunič, A. Golobič, M. Sanchez-Sanchez, A.J.W. Lobo, D.W. Lewis, D.S. Wragg, S. Nikitenko, W. Bras, B.M. Weckhuysen, *J. Phys. Chem. C* 115 (2011) 6331–6340.
- [51] W.K. Su, Z.G. Li, Y. Peng, J.H. Li, *Phys. Chem. Chem. Phys.* 17 (2015) 29142–29149.
- [52] L. Wondraczek, G. Gao, D. Möncke, T. Selvam, A. Kuhnt, W. Schwieger, D. Palles, E.I. Kamitsos, *J. Non-Cryst. Solids* 360 (2013) 36–40.
- [53] M.R.M.H.W. Mozgawa, *J. Mol. Struct.* 555 (2000) 351–356.
- [54] F. Gao, E.D. Walter, E.M. Karp, J. Luo, R.G. Tonkyn, J.H. Kwak, J. Szanyi, C.H.F. Peden, *J. Catal.* 300 (2013) 20–29.
- [55] A. Sultana, T. Nanba, M. Sasaki, M. Haneda, K. Suzuki, H. Hamada, *Catal. Today* 164 (2011) 495–499.
- [56] L. Xie, F. Liu, L. Ren, X. Shi, F.S. Xiao, H. He, *Environ. Sci. Technol.* 48 (2014) 566–572.
- [57] J. Hun Kwak, H. Zhu, J.H. Lee, C.H.F. Peden, J. Szanyi, *Chem. Commun. (Camb.)* 48 (2012) 4758–4760.
- [58] J. Luo, F. Gao, K. Kamasamudram, N. Currier, C.H.F. Peden, A. Yezersets, *J. Catal.* 348 (2017) 291–299.
- [59] T. Fjermestad, S. Svelle, O. Swang, *J. Phys. Chem. C* 117 (2013) 13442–13451.
- [60] A.A. Lamberov, A.M. Kuznetsov, M.S. Shapnik, A.N. Masliy, S.V. Borisevich, R.G. Romanova, S.R. Egorova, *J. Mol. Catal. A Chem.* 158 (2000) 481–486.
- [61] E. Lippmaa, A. Samoson, M. Magi, *J. Am. Chem. Soc.* 108 (1986) 1730–1735.
- [62] J. Klinowski, J.M. Thomas, C.A. Fyfe, G.C. Gobbi, *Nature* 296 (1982) 533–536.
- [63] H.E. van der Bij, B.M. Weckhuysen, *Chem. Soc. Rev.* 44 (2015) 7406–7428.
- [64] A. Corma, V. Fornes, W. Kolodziejki, L.J. Martinez-Triguero, *J. Catal.* 145 (1994) 27–36.
- [65] K. Xie, K. Leistner, K. Wijayanti, A. Kumar, K. Kamasamudram, L. Olsson, *Catal. Today* 297 (2017) 46–52.
- [66] C. Paolucci, A.A. Verma, S.A. Bates, V.F. Kispersky, J.T. Miller, R. Gounder, W.N. Delgass, F.H. Ribeiro, W.F. Schneider, *Angew. Chem. Int. Ed. Engl.* 53 (2014) 11828–11833.
- [67] A. Marberger, A.W. Petrov, P. Steiger, M. Elsener, O. Kröcher, M. Nachtegaal, D. Ferri, *Nat. Catal.* 1 (2018) 221–227.
- [68] T. Yu, J. Wang, Y. Huang, M. Shen, W. Li, J. Wang, *ChemCatChem* 6 (2014) 2074–2083.
- [69] L. Wang, W. Li, G. Qi, D. Weng, *J. Catal.* 289 (2012) 21–29.